Progress In Electromagnetics Research, Vol. 128, 519–537, 2012

MODIFIED CYLINDRICAL HOLOGRAPHIC ALGORITHM FOR THREE-DIMENSIONAL MILLIMETER-WAVE IMAGING

B. L. Ren, S. Y. Li*, H. J. Sun, W. D. Hu, and X. Lv

School of Information and Electronics, Beijing Institute of Technology, Beijing 100081, China

Abstract—Millimeter-wave (MMW) imaging techniques have been developed for the detection of concealed weapons and plastic explosives carried on personnel at major transportation hubs and secure locations. The combination of frequency-modulated continuous-wave (FMCW) technology and MMW imaging techniques leads to wideband, compact, and cost-effective systems which are especially suitable for security detection. Cylindrical three-dimensional (3-D) imaging technique, with the ability of viewing multiple sides, is an extension of rectilinear 3-D imaging technique only viewing a single side. Due to the relatively long signal sweep time, the conventional stop-and-go approximation of the pulsed systems is not suitable for FMCW systems. Therefore, a 3-D backscattered signal model including the effects of the continuous motion within the signal duration time is developed for cylindrical imaging systems. Then, a holographic image reconstruction algorithm, with motion compensation, is presented and demonstrated by means of numerical simulations.

1. INTRODUCTION

Personnel surveillance has been increasingly important due to the increasing threat of terrorism. Some modern threats, such as plastic or ceramic handguns and knives, as well as extremely dangerous liquid explosives, have emerged in recent years, which make the conventional security systems ineffective. Although some systems, such as X-ray systems and terahertz systems, can present effective solutions to this problem, X-ray systems [1] are unacceptable due to the potential health risks, and terahertz systems [2] are immature and too expensive for

Received 16 April 2012, Accepted 30 May 2012, Scheduled 8 June 2012

* Corresponding author: Shiyong Li (lisy_0723@hotmail.com).

civilian applications. Thus, we need a personnel surveillance system with the ability of detecting all types of modern threats cost-effectively and with the advantage of no harm to the person under surveillance. One of the choices is to use millimeter-wave which can penetrate common clothing barriers to form an image of a person as well as any concealed items with different reflectivity [3–5]. Millimeter waves are nonionizing and, therefore, pose no known health hazard at moderate power levels.

The combination of FMCW and MMW imaging techniques leads to wideband, compact, cost-effective, low-power operation, and high-quality imaging systems, which are especially suitable for security and detection application. FMCW signal has been widely used in imaging radar [6–9]. The continuous motion of the antenna while transmitting and receiving the signal for the FMCW systems is no longer negligible. Therefore, the stop-and-go approximation which is used in the conventional SAR imaging algorithms needs to be modified for FMCW image processing. Several conventional algorithms, such as wavenumber domain algorithm, frequency-scaling algorithm, range-Doppler algorithm and chirp-scaling algorithm, etc., have been modified to focus the FMCW SAR data [8, 10–12]. In [8], an accurate two-dimensional (2-D) received signal model was presented, in which a range-azimuth coupling term was formulated for the first time in the FMCW SAR community.

The rectilinear and cylindrical 3-D imaging techniques for concealed weapon detection were described along with several application results in [3, 13–17]. Wavenumber domain algorithms (or called range migration algorithms, abbreviated to RMA) [1, 13, 20] have been widely used in rectilinear 2-D and 3-D imaging system. Cylindrical 3-D imaging technique is an extension of rectilinear imaging technique. A cylindrical holographic algorithm was first developed by Soumekh [18, 19] and was used for security imaging by Sheen et al. [15]. A 3-D RMA was developed for cylindrical geometries by backpropagating the backscattered data onto a planar aperture in [21].

Cylindrical 3-D imaging technique has the ability of viewing multiple sides [14], so we choose it for personal security detection. The radius of the scan should be generally on the order of 1 m, obviously in the near-field of millimeter-wave imaging for personnel surveillance. The cylindrical algorithms mentioned above are generally used without considering the effects of the continuous motion within the signal duration time. In this paper, we analyze the 3-D signal model which takes the characteristics of FMCW systems into account. The main effects of the motion on the image result turn out to be a range walk and out of focus. These effects can be compensated for

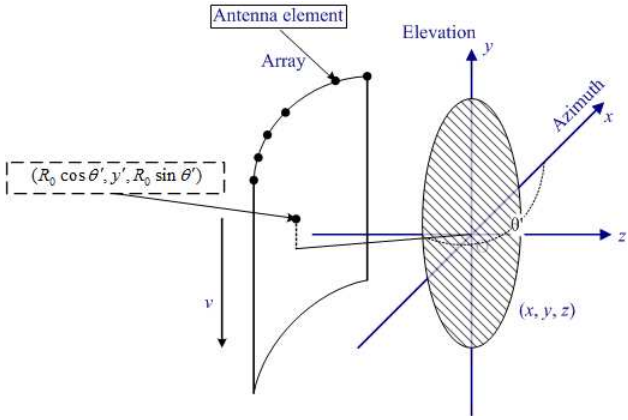

Figure 1. Near-field 3-D imaging configuration.

by a matched filter multiplication in the 3-D wavenumber domain. Then, a deconvolution of the Green's function is performed. After the corrections, the range curvature of all scatterers having the same minimum range as the scatterer at the reference range is corrected exactly . The residual curvature of the scatterers at other locations is compensated for by implementing the bilinear mapping from the polar format to rectangular format. The complex image can then be reconstructed by the 3-D inverse fast Fourier transform (IFFT).

This paper is organized as follows. In Section 2, an accurate backscattered signal model and the imaging algorithm are presented. The 3-D imaging procedure is given in Section 3. Section 4 shows the simulation results to verify the effectiveness of the motion compensation. Section 5 summarizes the conclusions.

2. FMCW THREE-DIMENSIONAL SIGNAL MODEL AND IMAGING ALGORITHM

This section derives a holographic imaging algorithm based on the analytical model of the FMCW backscattered signal in the 3-D wavenumber domain for cylindrical imaging systems. The 3-D imaging geometry is shown in Figure 1. The one-dimensional (1-D) arc antenna array aligned with the azimuth direction is scanned along the minus y direction.

The transmitted FM signal can be expressed as [22]:

$$s_T(t) = \exp\left[j2\pi\left(f_0 t + \frac{1}{2}Kt^2\right)\right], \tag{1}$$

where f_0 is the carried base frequency, t is the time variable varying within one cycle of signal transmitting, and K is the frequency sweep

rate of the transmitted signal.

Assuming that the signal is transmitted at an arbitrary time τ and received at time $\tau + \tau_d$. The time τ_d is the round-trip delay time. The corresponding instantaneous ranges between the antenna element and the target are $R(\tau)$ and $R(\tau + \tau_d)$, respectively. Consequently, the round-trip delay time can be expressed as

$$\tau_d = \frac{R(\tau) + R(\tau + \tau_d)}{c}, \tag{2}$$

where

$$\begin{aligned} R(\tau) &= \sqrt{(R_0 \cos\theta' - x)^2 + (y' - y)^2 + (R_0 \sin\theta' - z)^2} \\ &= \sqrt{(R_0 \cos\theta' - x)^2 + (y'_0 - v\tau - y)^2 + (R_0 \sin\theta' - z)^2}, \\ R(\tau+\tau_d) &= \sqrt{(R_0 \cos\theta' - x)^2 + (y' - y)^2 + (R_0 \sin\theta' - z)^2} \\ &= \sqrt{(R_0 \cos\theta' - x)^2 + [y'_0 - v(\tau+\tau_d) - y]^2 + (R_0 \sin\theta' - z)^2}, \\ y' &= {y'}_0 - v\tau, \\ \tau = nT_{\theta'} + mT_y v + t, &\quad n = 0, 1, \ldots N-1, \quad m = 0, 1, \ldots M-1, \quad t \in (0, T_{\theta'}) \end{aligned}$$

and c is the speed of light, y'_0 represents the starting scanning position of the arc antenna array, R_0 is the radius of the arc antenna array, v is the scanning velocity and τ is the continuous time. (x, y, z) is the location of a point target in a 3-D Cartesian coordinate system. And $(R_0 \cos\theta', y', R_0 \sin\theta')$ is the position of the antenna element, where y' represents the scanning position of the arc antenna array, θ' represents the angle in the cylindrical coordinate system as shown in Figure 1 . The origins of the two coordinate systems are the same. The period of signal transmitting along the arc array elements in the azimuth domain is $T_{\theta'}$ which is assumed to be equal to the pulse repetition interval. T_y is the period of sampling time along y direction. The number of the array elements is N corresponding to the number of samples along the azimuth direction. M is the number of samples along elevation direction.

Owing to the fact that the distance between the antenna array and the target is very short for the personnel security detection, (2) is accurately approximated as

$$\tau_d \approx \frac{2R(\tau)}{c}. \tag{3}$$

Neglecting the time scaling influences on the envelope, the received signal from a single point target can be expressed as

$$s_R(\theta', y'; t) = \sigma(x, y, z)\, s_T(t - \tau_d), \tag{4}$$

where $\sigma(x, y, z)$ is the reflectivity of the single point target.

In dechirp-on-receive SAR systems, the received signal is mixed with a reference signal in order to reduce the sampling requirements and data rates [22]. The reference signal is a version of the transmitted signal with delayed time τ_c. The dechirped signal can be written as

$$s_{\mathrm{IF}}\left(\theta', y'; t\right) = \sigma(x, y, z) \exp\left[-j2\pi f_0 (\tau_d - \tau_c)\right] \exp[-j2\pi K (\tau_d - \tau_c)(t - \tau_c)] \exp\left[j\pi K (\tau_d - \tau_c)^2\right]. \quad (5)$$

The last exponential term of (5) is known as the residual video phase (RVP), which is introduced by the operation of the dechirp-on-receive technology [22]. The compensation for RVP is conducted in the frequency domain, which has been introduced in [23]. Assuming the RVP has been removed in the remainder of the derivation, i.e.,

$$s_{\mathrm{IF}}\left(\theta', y'; t\right) = \sigma(x, y, z) \exp[-j2\pi f_0 (\tau_d - \tau_c)] \exp[-j2\pi K (\tau_d - \tau_c)(t - \tau_c)]. \quad (6)$$

Substituting $f = K(t - \tau_c)$ into (6), we obtain

$$s_{\mathrm{IF}}\left(\theta', y'; f\right) = \sigma(x, y, z) \exp\left[-j2\pi(f + f_0)(\tau_d - \tau_c)\right]. \quad (7)$$

Applying the substitution of $\tau = mT_y + nT_{\theta'} + t = \tau_m + \tau_n + t$ to (7):

$$s_{\mathrm{IF}}\left(\theta', f, y'; \tau_m, \tau_n, t\right) = \sigma(x, y, z) \exp\left[-j4\pi(f + f_0)\left(\frac{R(\tau_m + \tau_n + t)}{c} - \frac{R_c}{c}\right)\right], \quad (8)$$

where $R_c = c\tau_c/2$.

In order to obtain the reflectivity $\sigma(x, y, z)$,we should first give the Fourier analysis of the function $s_{\mathrm{IF}}(\theta', f, y'; \tau_m, \tau_n, t)$ in the elevation frequency domain.

So performing 1-D Fourier transform to (8) with respect to the spatial variables y'_m ($y'_m = v\tau_m = vmT_y$), yields

$$S_{\mathrm{IF}}\left(\theta', f, k'_y; \tau_n, t\right) = \frac{1}{v}\int s_{\mathrm{IF}}\left(\theta', f; y'_m, \tau_n, t\right) \exp\left(-jk_{y'} y'_m\right) dy'_m = \frac{1}{v}\sigma(x, y, z) \int \exp\left[-j\Phi\left(\theta', k_r, k_{y'}; y'_m, \tau_n, t\right)\right] dy'_m, \quad (9)$$

where

$$\Phi\left(\theta', k_r, k_{y'}; y'_m, \tau_n, t\right) = \frac{4\pi(f + f_0)}{c}\left[R(\tau_m + \tau_n + t) - R_c\right] + k_{y'} y'_m = 2k_r\left[R(\tau_m + \tau_n + t) - R_c\right] + k_{y'} y'_m$$

and $k_r = 2\pi(f + f_0)/c$.

The above integral can be evaluated by applying the principle of the stationary phase method [19, 22, 24]. At the point of stationary phase, the phase $\Phi\left(\theta',\, k_r,\, k_{y'};\, y'_m,\, \tau_n,\, t\right)$ takes an extreme value, such as

$$\left.\frac{\partial\Phi\left(\theta', k_r, k_{y'}; y'_m, \tau_n, t\right)}{\partial y'_m}\right|_{y'_m=y'_{m_0}} = 0, \tag{10}$$

$$\left.\frac{\partial^2\Phi\left(\theta', k_r, k_{y'}; y'_m, \tau_n, t\right)}{\partial^2 y'_m}\right|_{y'_m=y'_{m_0}} \neq 0. \tag{11}$$

Solving (10) for the stationary phase point y'_{m0}, yields

$$\begin{aligned}&\left(4k_r^2 - k_{y'}^2\right)\left[y'_{m0} + v\left(\tau_n + t\right) - \left(y'_0 - y\right)\right]^2\\ &= k_{y'}^2\left[\left(R_0\cos\theta' - x\right)^2 + \left(R_0\sin\theta' - z\right)^2\right].\end{aligned}$$

After derivation, we can obtain

$$\begin{aligned}y'_{m_0} &= -y + y'_0 - v\tau_n - \frac{k_{y'}R_{xz}}{\sqrt{4k_r^2 - k_{y'}^2}} - vt\\ &= -y - \frac{k_{y'}R_{xz}}{\sqrt{4k_r^2 - k_{y'}^2}} + y'_0 - v\tau_n - vt,\end{aligned} \tag{12}$$

where

$$R_{xz} = \sqrt{(R_0\cos\theta' - x)^2 + (R_0\sin\theta' - z)^2}. \tag{13}$$

If the point target is positioned at the center of the coordinates and $y' \in (-L,\, L)$, then

$$k_{y'} \in \left(-2k_r\frac{L}{\sqrt{R_0^2 + L^2}}, 2k_r\frac{L}{\sqrt{R_0^2 + L^2}}\right)$$

and $2L$ is the size of the elevation synthetic aperture [18].

Then (9) can be expressed as

$$\begin{aligned}S_{\mathrm{IF}}\left(\theta', k_r, k_{y'}; \tau_n, t\right) = \frac{1}{v}\sigma(x,y,z)\exp\Big\{-j\Big[&-k_{y'}y + k_{y'}\left(y'_0 - v\tau_n - vt\right)\\ &-2k_rR_c + R_{xz}\sqrt{4k_r^2 - k_{y'}^2}\Big]\Big\}.\end{aligned} \tag{14}$$

Consequently, by the substitution of $t = f/K + 2R_c/c$, (14) can also be rewritten as

$$\begin{aligned}S_{\mathrm{IF}}\left(\theta', k_r, k_{y'}; \tau_n\right) = \frac{1}{v}\sigma(x,y,z)\exp\Bigg\{-j\Bigg[&-k_{y'}y + k_{y'}y'_0 - k_{y'}v\tau_n - k_{y'}v\frac{f}{K}\\ &-k_{y'}v\frac{2R_c}{c} - 2k_rR_c + R_{xz}\sqrt{4k_r^2 - k_{y'}^2}\Bigg]\Bigg\}.\end{aligned} \tag{15}$$

The minus in "$-k_{y'}y$" is introduced by the scanning direction of the array.

For a volume target we can write

$$S_{\mathrm{IF}}\left(k_{y'},k_r;\theta'\right)=\int\limits_x\int\limits_y\int\limits_z\frac{1}{v}\sigma(x,y,z)\times\exp\left\{-j\left[-k_{y'}y+k_{y'}y_0'-k_{y'}v\tau_n\right.\right.$$

$$\left.\left.-k_{y'}v\frac{f}{K}-k_{y'}v\frac{2R_c}{c}-2k_rR_c+R_{xz}\sqrt{4k_r^2-k_{y'}^2}\right]\right\}dxdydz$$

$$=\exp\left\{-j\left[k_{y'}y_0'-k_{y'}v\tau_n-k_{y'}v\frac{f}{K}-k_{y'}v\frac{2R_c}{c}-2k_rR_c\right]\right\}\times\iiint\limits_{x\,y\,z}\frac{1}{v}\sigma(x,y,z)$$

$$\exp(jk_y'y)\exp[-jk_{xz}\sqrt{(R_0\cos\theta'-x)^2+(R_0\sin\theta'-y)^2}]dxdydz,\quad(16)$$

where $k_{xz}=\sqrt{4k_r^2-k_{y'}^2}$.

The above model can be given by

$$S_{\mathrm{IF}}\left(k_{y'},k_r;\theta'\right)=\frac{1}{v}\exp\left\{-j\left[k_{y'}y_0'-k_{y'}v\tau_n-k_{y'}v\frac{f}{K}-k_{y'}v\frac{2R_c}{c}-2k_rR_c\right]\right\}$$

$$\times\int\limits_x\int\limits_z F_y(x,z,k_{y'})g_{\theta'}^*(k_{xz},x,z)dxdz,\qquad(17)$$

where

$$F_y(x,z,k_{y'})=\int\limits_y\sigma(x,y,z)\exp(jk_{y'}y)dy$$

and

$$g_{\theta'}(k_{xz},x,z)=\exp\left[jk_{xz}\sqrt{(R_0\cos\theta'-x)^2+(R_0\sin\theta'-z)^2}\right].$$

Based on the generalized Parseval's theorem [18, 19], this model can be expressed as

$$S_{\mathrm{IF}}\left(k_{y'},k_r;\theta'\right)=\frac{1}{v}\exp\left\{-j\left[k_{y'}y_0'-k_{y'}v\tau_n-k_{y'}v\frac{f}{K}-k_{y'}v\frac{2R_c}{c}-2k_rR_c\right]\right\}$$

$$\times\int\limits_{k_x}\int\limits_{k_z}F_(k_x,k_z,k_{y'})G_{\theta'}^*(k_{xz},k_x,k_z)dk_xdk_z.\qquad(18)$$

Transforming the above double integral into the polar coordinate in

the wavenumber domain, one can obtain

$$S_{\mathrm{IF}}(k_{y'}, k_r; \theta') = \frac{1}{v}\exp\left\{-j\left[k_{y'}y'_0 - k_{y'}v\tau_n - k_{y'}v\frac{f}{K} - k_{y'}v\frac{2R_c}{c} - 2k_rR_c\right]\right\} \times \int_{k_{xz}} k_{xz}\left[\int_{\phi} F_{k_{xz}}(k_{xz}, \phi, k_{y'})G^*_{\theta' k_{xz}}(k_{xz}, \theta' - \phi)d\phi\right]dk_{xz}. \quad (19)$$

Using the Fourier properties of circular symmetric function [18, 19], we have

$$G_{\theta' k_{xz}}(k_{xz}, \phi) = \exp[jk_{xz}R_0\cos(\phi)].$$

The term inside the [ ] of (19) represents a convolution in the θ' domain, such as

$$\int_{\phi} F_{k_{xz}}(k_{xz}, \phi, k_{y'})G^*_{\theta' k_{xz}}(k_{xz}, \theta' - \phi)d\phi = F_{k_{xz}}(k_{xz}, \theta', k_{y'}) \otimes G^*_{k_{xz}}(k_{xz}, \theta').$$

Based on the derivation in [18, 19], yields

$$F_{k_{xz}}(k_{xz}, \theta', k_{y'}) = v * \mathrm{IFFT}_{(\theta')}\left\{\frac{\mathrm{FFT}_{(\theta')}\left\{S_{\mathrm{IF}}(k_{y'}, k_r; \theta')\exp\left[j\Phi(k_{y'}, k_r; f)\right]\right\}}{\mathrm{FFT}_{(\theta')}\left[G^*_{k_{xz}}(k_{xz}, \theta')\right]}\right\}, \quad (20)$$

where

$$S'_{\mathrm{IF}}(k_{y'}, k_r; \theta') = S_{\mathrm{IF}}(k_{y'}, k_r; \theta')\exp\left[j\Phi(k_{y'}, k_r; f)\right]$$

and

$$\Phi(k_{y'}, k_r; f) = k_{y'}y'_0 - k_{y'}v\tau_n - k_{y'}v\frac{f}{K} - k_{y'}v\frac{2R_c}{c} - 2k_rR_c. \quad (21)$$

Note that the first term $k_{y'}y'_0$ in (21) is introduced by the initial position of the array. The term $k_{y'}v\tau_n$ represents the phase variation corresponding to the elevation-range walk caused by the motion of the nth antenna element. $k_{y'}vf/K$ is a space-invariant term also caused by the motion of the array within the sweep time. The terms $k_{y'}v(2R_c/c)$ and $2k_rR_c$ refer to the constant shifts of the azimuth and range, respectively, and are introduced by the dechirp-on-receive technology.

After the reference function multiplication (RFM), we can obtain $F_{k_{xz}}(k_{xz}, \theta', k_{y'})$ as shown in (20). The process of RFM is discussed in detail in Section 3.

The cylindrical samples of $F_{k_{xz}}(k_{xz}, \theta', k_{y'})$ are then converted to the samples of $F(k_x, k_z, k_{y'})$via an interpolation algorithm, where

$$k_x = k_{xz}\cos\theta,$$
$$k_z = k_{xz}\sin\theta,$$
$$k_y = k_{y'}.$$

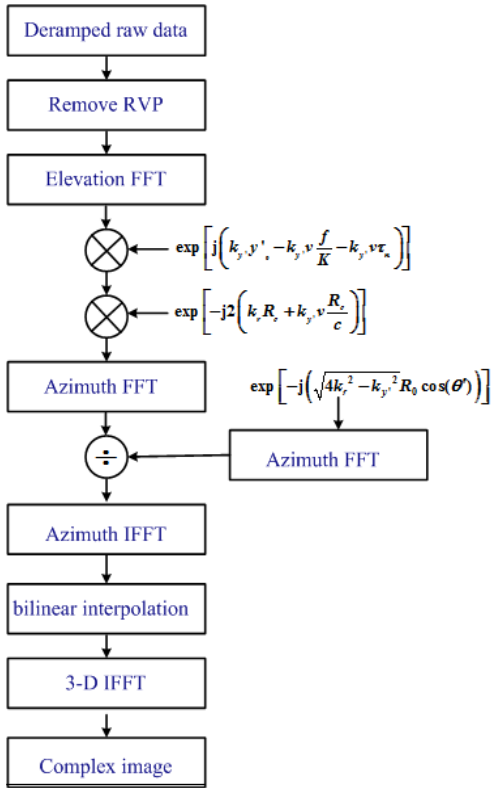

Figure 2. Flow diagram of the proposed image reconstruction method.

The distinction between the primed and unprimed coordinate systems can now be dropped since the coordinate systems coincide. Since $\sigma(x, y, z)$ and $F(k_x, k_y, k_z)$ form a Fourier transform pair, the 3-D inverse Fourier transform of this signal is the desired image, i.e.,

$$\sigma(x,y,z)=v\iiint F(k_x,k_y,k_z)\exp[j\,(k_x x-k_y y+k_z z)]\,dk_x dk_y dk_z. \quad (22)$$

The constant factor relative to 2π is ignored in (22).

3. THREE-DIMENSIONAL IMAGING PROCEDURE

The computational procedure of the algorithm which is proposed in Section 2 is summarized in Figure 2 and is outlined in detail in the following steps.

Step 1: Remove RVP. Removing RVP is not the key parts in this paper, so it is not addressed.

Step 2: Perform the fast Fourier transform (FFT) of $s_{\mathrm{IF}}(\theta', y'; f)$ acquired in step 1 with respect to y' for each frequency and azimuth angle. As a result, the raw data in the y' domain is transformed into the $k_{y'}$ domain.

Step 3: RFM. Corrections of the phase are the emphasis of this paper. The processing steps of the matched filtering can be split into two parts.

1) Remove the unwanted phase in the wavenumber domain.

a) Considering the motion within the sweep, a 3-D matched filter is given by

$$G_F\left(k_{y'}, k_r; \tau_n\right) = \exp\left[j\left(k_{y'}y'_0 - k_{y'}v\frac{f}{K} - k_{y'}v\tau_n\right)\right] \exp\left[j\left(-2k_rR_c - k_{y'}v\frac{2R_c}{c}\right)\right]. \quad (23)$$

b) Under the stop-and-go approximation, the conventional matched filter [22] is shown as follows

$$G_F\left(k_{y'}, k_r; \tau_n\right) = \exp\left[j\left(-2k_rR_c - k_{y'}v\frac{2R_c}{c}\right)\right]. \quad (24)$$

Note that the term $k_{y'}v\tau_n$ exists in the elevation-frequency domain and the azimuth-time domain, therefore the term G_F should be first multiplied exactly before the azimuth Fourier transform and after the elevation Fourier transform, as shown in Figure 2.

2) Correct the range curvature of all scatterers at the reference range R_0.

In this paper, R_0 is considered as the reference range. The correction progress should be calculated in the $k_{\theta'}$ domain in the proposed algorithm, such as the following steps.

a) Calculate the FFT of $S'_{\mathrm{IF}}(k_{y'}, k_r; \theta')$ acquired in step 3 with respect to θ', so the function $S'_{\mathrm{IF}}(k_{y'}, k_r; k_{\theta'})$ is obtained.

b) Obtain the FFT of the function $G^*_{k_{xz}}(k_{xz}, \theta')$ with respect to θ', so as to yield the function $G^*_{k_{xz}}(k_{xz}, k_{\theta'})$.

c) Take the complex product of $S'_{\mathrm{IF}}(k_{y'}, k_r; k_{\theta'})$ and $1/G^*_{k_{xz}}(k_{xz}, k_{\theta'})$ in the $k_{\theta'}$ domain.

d) Perform the IFFT of the product with respect to $k_{\theta'}$ in order to obtain $F_{k_{xz}}(k_{xz}, \theta', k_{y'})$.

In order to further alleviate the computational load of the algorithm, the term $1/G^*_{k_{xz}}(k_{xz}, k_{\theta'})$ which is defined as the focusing function [17] in this paper can be calculated first and stored in memory.

The focusing function is multiplied to correct the range curvature of all scatterers at the reference range. Residual range curvature is still present on those scatterers which are not located at the reference range [18, 22]. The residual range curvature is compensated for by implementing the bilinear mapping, which will be shown in step 4.

Step 4: Use bilinear interpolation to convert $F_{k_{xz}}(k_{xz}, \theta', k_{y'})$ into a 3-D linear phase grating. The relationship of the variables is

$$\begin{aligned} k_{xz}\cos\theta &= \sqrt{4k_r^2 - k_y^2}\cos\theta \to k_x, \\ k_{xz}\sin\theta &= \sqrt{4k_r^2 - k_y^2}\sin\theta \to k_z, \end{aligned} \tag{25}$$

where $k_x s$ and $k_z s$ are uniformly spaced.

Step 5: Perform 3-D IFFT operation on the uniformly spaced wavenumber domain data $F(k_x, k_y, k_z)$. As a result, the 3-D reflectivity image $\sigma(x, y, z)$ is obtained.

In [25], a modified rectilinear 3-D FMCW SAR imaging algorithm is presented. The main difference between the rectilinear imaging algorithm and the cylindrical imaging algorithm is that a convolution in the azimuth domain is needed for the latter. And another difference is that the cylindrical imaging algorithm needs bilinear interpolation to compensate the residual curvature, however, the rectilinear imaging algorithm needs 1-D interpolation.

4. SIMULATION RESULTS

In order to validate the performance of the modified holographic algorithm, two numerical simulations have been carried out. The simulation parameters used in this paper are listed in Table 1.

Table 1. Simulation Parameters.

Parameter	Value
Carrier frequency	35 GHz
Bandwidth	5 GHz
Sampling interval: $\Delta\theta'$	0.007 rad
Number of array elements	64
Sampling interval: $\Delta y'$	0.007 m
Number of samples along y direction	64
Scanning velocity	1 m/s
Referenced range R_0	1 m

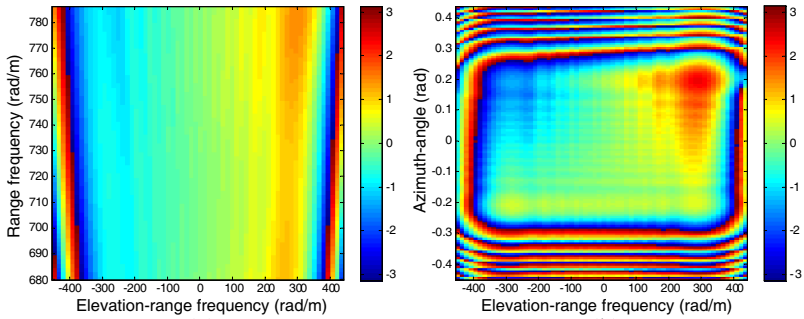

Figure 3. Phase of the signal for a single point target in the scene center after matched filtering with a reference function based on the stop-and-go approximation. (a) Phase in the elevation-frequency and range-frequency domain. (b) Phase in the elevation-frequency and azimuth-angle domain.

The target used in the first simulation is a single point target, and we can get the point spread function (PSF) of the target with cylindrical aperture. The wavenumber domain data $S_{\mathrm{IF}}(k_{y'}, k_r; \theta')$ in (20) is multiplied by the conventional and the proposed matched filters which are shown in (23) and (24), respectively.

Figure 3 shows the phase of the signal after step 3 in Section 3 with the matched filtering function that makes the stop-and-go approximation. The phase of the remaining signal in the elevation-frequency and range-frequency domain after step 3 is illustrated in Figure 3(a), and the phase in the elevation-frequency and azimuth-angle domain, is shown in Figure 3(b). The phase in the azimuth-angle and range-frequency domain is not demonstrated due to the fact that it is not affected by the motion of the sweep, as shown in Figure 1.

Figure 4 illustrates the phase results after step 3 produced by filtering the signal $S_{\mathrm{IF}}(k_{y'}, k_r; \theta')$ with the proposed function in (23).

If the signal $S_{\mathrm{IF}}(k_{y'}, k_r; \theta')$ is completely compensated for by the matched filter, the phase of the remaining signal should be constant and do not vary with θ', $k_{y'}$ and k_r in the case that the simulated point target is in the scene center, i.e., $(x, y, z) = (0, 0, 0)$. Clearly, only in Figure 4 does the phase in the support band is practically constant, indicating that the matched filter does match the received signal.

Figures 5(a) to (c) show the PSF of a single point target located in the scene center corresponding to the x-y (with $z = 0$), y-z (with $x = 0$), and x-z (with $y = 0$) section planes, respectively, with the matched filtering function based on the stop-and-go approximation. It can be seen that a range walk exists in the elevation direction which is

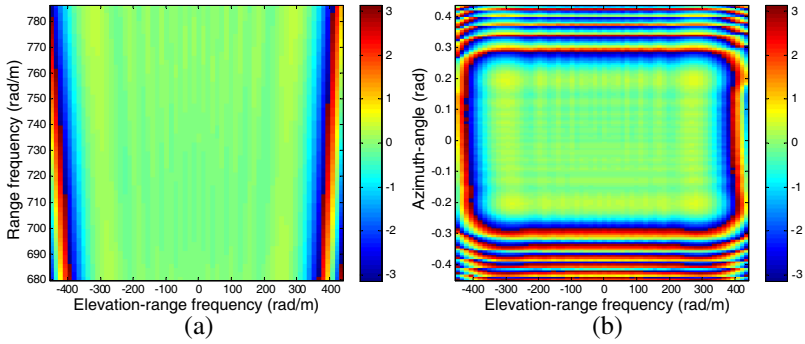

Figure 4. Phase of the signal for a single point target in the scene center after matched filtering with the proposed function in (23). (a) Phase in the elevation-frequency and range-frequency domain. (b) Phase in the elevation-frequency and azimuth-angle domain.

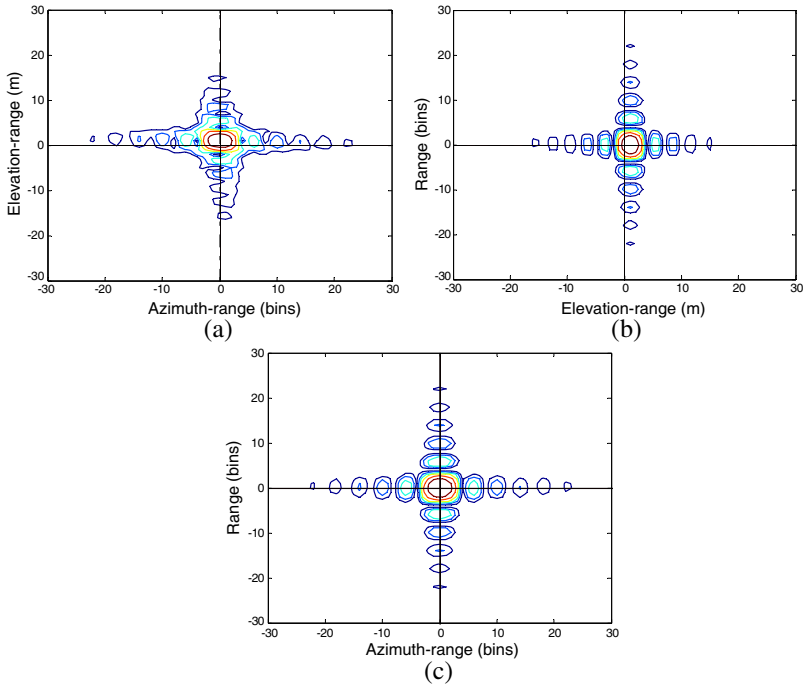

Figure 5. The PSF images in the x-y (with $z = 0$), y-z (with $x = 0$), and x-z (with $y = 0$) section planes, respectively, with the matched filtering function based on the stop-and-go approximation. (a) Image in the x-y section plane. (b) Image in the y-z section plane. (c) Image in the x-z section plane.

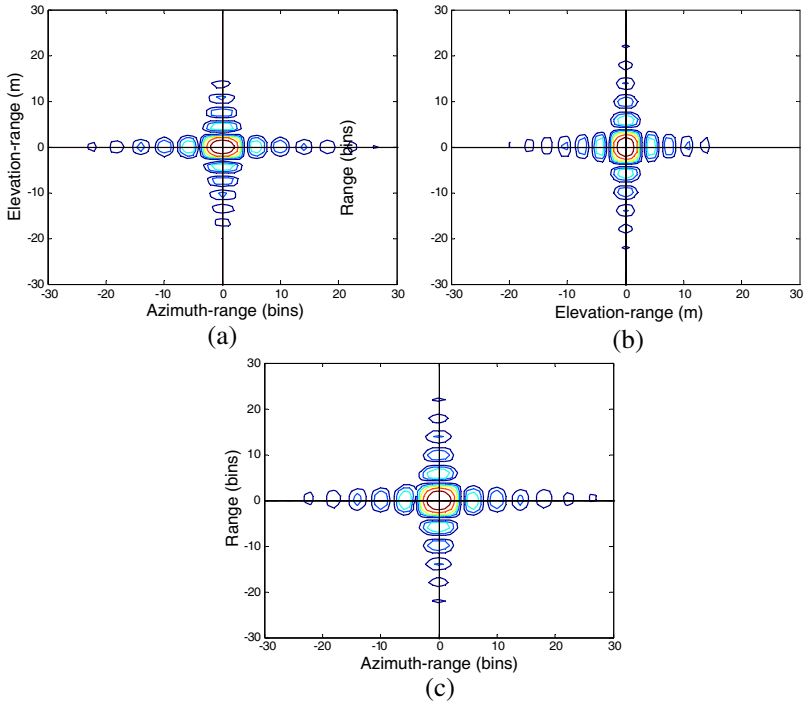

Figure 6. The PSF images in the x-y (with $z = 0$), y-z (with $x = 0$), and x-z (with $y = 0$) section planes, respectively, with the proposed matched filtering function. (a) Image in the x-y section plane. (b) Image in the y-z section plane. (c) Image in the x-z section plane.

caused by the motion of the array, as shown in Figures 5(a) and (b). The motion is not affected the image in the x-z plane in Figure 5(c).

Figures 6(a) to (c) demonstrate the corresponding image results produced by the proposed matched filtering function in (23). It can be seen from Figures 5 and 6 that the improvements due to the proposed correction are visible. The loss of the peak power and the elevation-range walk are compensated by the proposed algorithm and the sidlobes of the PSF in Figure 6(a) are more similar to the sidelobes of the ideal sinc function. In order to show the improvements clearly, the simulation has been carried out for different platform velocities from 0.5–1 m/s. As can be seen from Figures 7(a) and 7(c), the peak level is below 0 dBm^2 at higher velocities. The loss of peak power is 0.5 dBm^2 at 1 m/s. However, no peak power is lost at any platform velocities in Figures 7(b) and 7(d). The elevation-range walk is $v/2f_s$ (f_s is the sampling rate), which is compensated by the proposed algorithm as shown in Figures 6(a), 7(b) and 7(d).

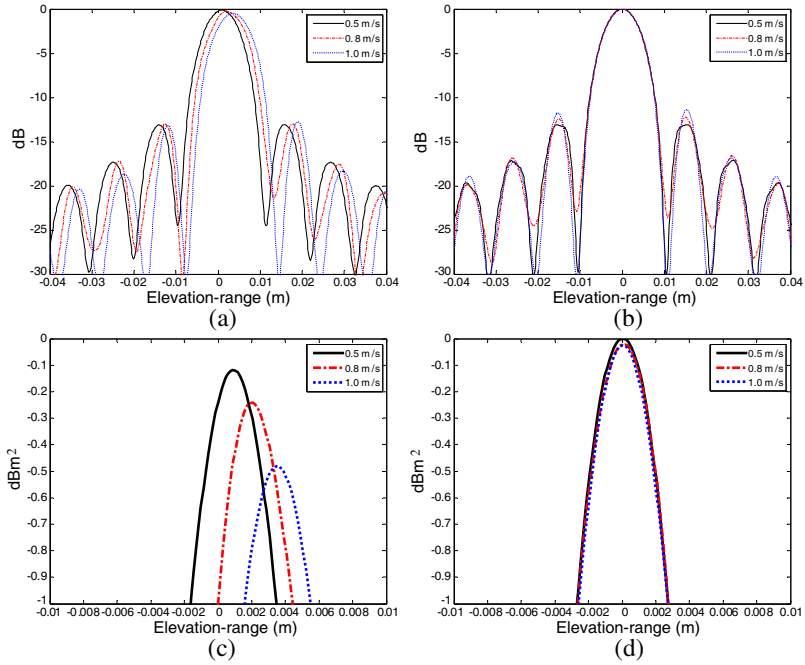

Figure 7. The PSF images in the y (with $x = 0$ and $z = 0$) dimension at different platform velocities from 0.5–1 m/s, (a) with the stop-and-go approximation and (b) with the proposed matched filtering function. (c) and (d) are the enlargements of the main lobe in (a) and (b), respectively.

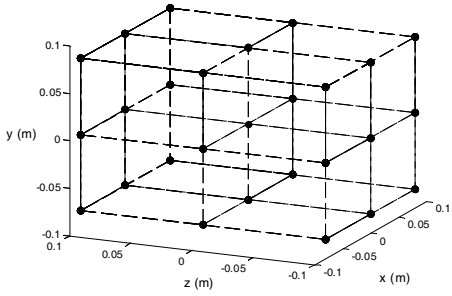

Figure 8. The cuboid target model consisting of 27 scatterers.

In order to verify the efficiency of the proposed algorithm for the targets with multiple scattering centers, we have given a simulation of a cuboid target model consisting of 27 scatterers in Figure 8. The

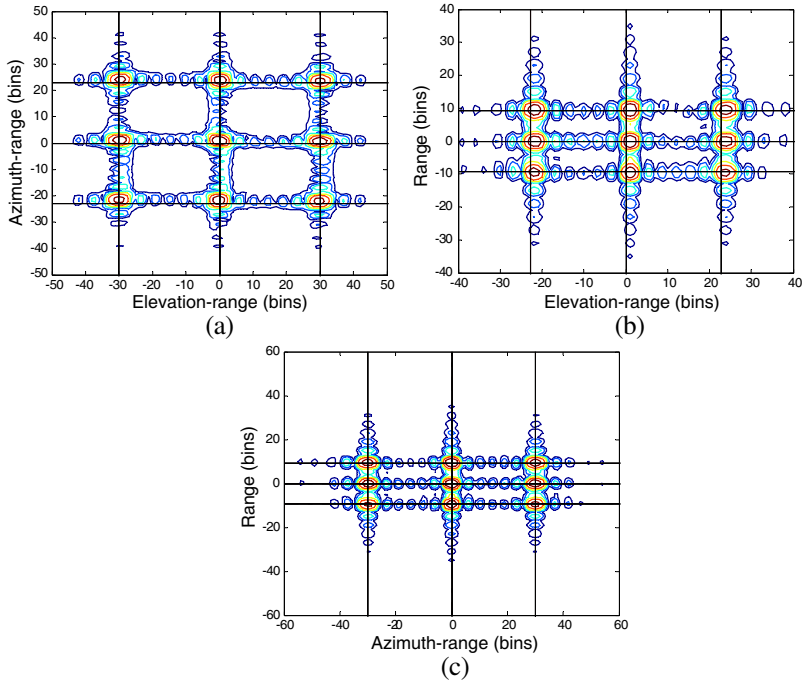

Figure 9. Projections of the 3-D image of the cuboid target model onto the x-y, y-z and x-z planes, respectively, with the matched filtering function based on the stop-and-go approximation. (a) Projections onto the x-y plane. (b) Projections onto the y-z plane. (c) Projections onto the x-z plane.

size of the cuboid target model is 0.16 m × 0.16 m × 0.2 m. The interval of the points is 0.1 m in the range dimension and 0.08 m in the elevation-range and azimuth-range dimensions. The radar cross section (RCS) of all scatterers is 1 m^2. The projections of the images onto the three main planes are shown in Figures 9 and 10, with the matched filtering function using the stop-and-go approximation and the proposed matched filtering function respectively. The real positions of the scatterers are represented by the intersections of the dashed lines. The defocusing and range walk are clearly seen in Figure 9 and are the same as shown in Figure 5. Figure 10 shows that the focusing performance of the proposed algorithm is improved. The range walk in the elevation-range dimension is compensated and the sidelobes of the image in Figure 10(a) are more similar to the sidelobes of the ideal sinc function. The dynamic range of the images is 30 dB.

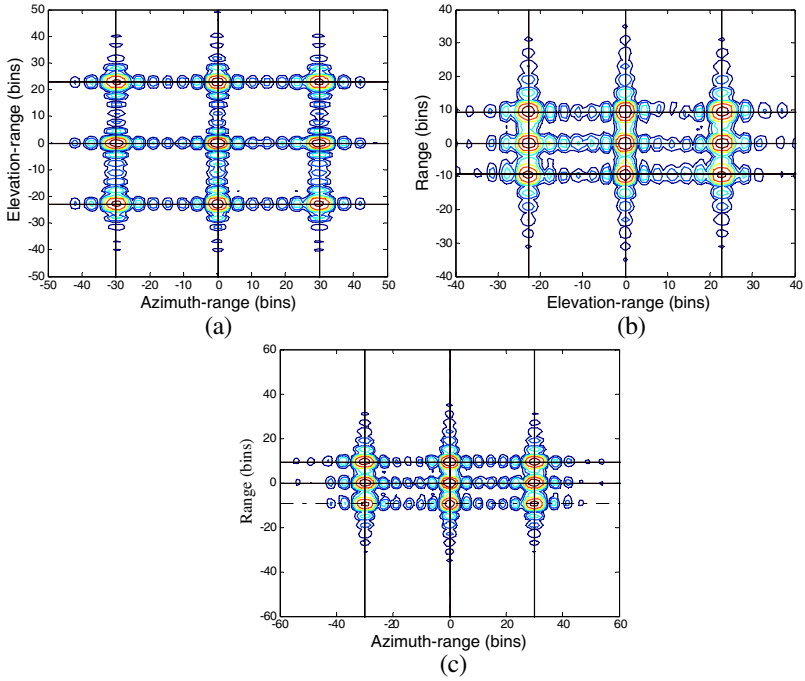

Figure 10. Projections of the 3-D image of the cuboid target model onto the x-y, y-z and x-z planes, respectively, with the proposed matched filtering function. (a) Projections onto the x-y plane. (b) Projections onto the y-z plane. (c) Projections onto the x-z plane.

5. CONCLUSIONS

A holographic imaging algorithm with motion compensation to process the near-field 3-D imaging for cylindrical imaging systems has been developed. In this algorithm, the effects of the array motion during the long pulse duration have been described and compensated for. The additional terms caused by the motion have been removed. In order to accelerate the image reconstruction process, the focusing function can be calculated first and stored in memory. Numerical simulations show that the focusing performance of the proposed algorithm is improved.

REFERENCES

1. Currie, N. C., F. J. Demma, D. D. Ferris, Jr., R. W. McMillian, and M. C. Wicks, "ARPA/NIJ/Rome Laboratory concealed weapon detection program: An overview," *Proceedings of SPIE*, Vol. 2755, 492–502, Orlando, Florida, USA, Apr. 1996.
2. Cooper, K. B., R. J. Dengler, N. Llombart, et al., "Penetrating 3-D

imaging at 4- and 25-m range using a submillimeter-wave radar," *IEEE Trans. on Microwave Theory and Techniques*, Vol. 56, No. 12, 2771–2778, Dec. 2008.

3. Sheen, D. M., D. L. McMakin, and T. E. Hall, "Three-dimensional millimeter-wave imaging for concealed weapon detection," *IEEE Trans. on Microwave Theory and Techniques*, Vol. 49, No. 9, 1581–1592, Sep. 2001.
4. Appleby, R. and R. N. Anderton, "Millimeter-wave and submillimeter-wave imaging for security and surveillance," *Proceedings of the IEEE*, Vol. 95, No. 8, 1683–1690, Aug. 2007.
5. Yeom, S., D. Lee, H. Lee, J. Son, and V. P. Gushin, "Distance estimation of concealed objects with stereoscopic passive millimeter-wave imaging," *Progress In Electromagnetics Research*, Vol. 115, 399–407, 2011.
6. Huang, Y., P. V. Brennan, D. Patrick, I. Weller, P. Roberts, and K. Hughes, "FMCW based MIMO imaging radar for maritime navigation," *Progress In Electromagnetics Research*, Vol. 115, 327–342, 2011.
7. Meta, A., P. Hoogeboom, and L. P. Ligthart, "Signal processing for FMCW SAR," *IEEE Trans. on Geoscience and Remote Sensing*, Vol. 45, No. 11, 3519–3532, Nov. 2007.
8. Wang, R., O. Loffeld, H. Nies, S. Knedlik, M. Hagelen, and H. Essen, "Focus FMCW SAR data using the wavenumber domain algorithm," *IEEE Trans. on Geoscience and Remote Sensing*, Vol. 48, No. 4, 2109–2118, Apr. 2010.
9. Lee, M. S., "Signal modeling and analysis of a planar phased-array FMCW radar with antenna switching," *IEEE Antennas and Wireless Propagation Letters*, Vol. 10, 179–182, 2011.
10. Mittermayer, J., A. Moreira, and O. Loffeld, "Spotlight SAR data processing using the frequency scaling algorithm," *IEEE Trans. on Geoscience and Remote Sensing*, Vol. 37, No. 5, 2198–2214, Sep. 1999.
11. De Wit, J. J. M., A. Meta, and P. Hoogeboom, "Modified range-doppler processing for FM-CW synthetic aperture radar," *IEEE Geoscience and Remote Sensing Letters*, Vol. 3, No. 1, 83–87, Jul. 2006.
12. Jiang, Z. H., K. Huang-Fu, and J. W. Wan, "A chirp transform algorithm for processing squint mode FMCW SAR data," *IEEE Geoscience and Remote Sensing Letters*, Vol. 4, No. 3, 377–381, Jul. 2007.
13. Sheen, D. M., H. D. Collins, T. E. Hall, D. L. McMakin,

R. P. Gribble, R. H. Severtsen, J. M. Prince, and L. D. Reid, "Real-time wideband holographic surveillance system," US Patent 5557283, Sep. 17, 1996.

14. Sheen, D. M., D. L. McMakin, T. E. Hall, and R. H. Severtsen, "Real-time wideband cylindrical holographic surveillance system," US Patent 5859609, Jan. 12, 1999.
15. Sheen, D. M., D. L. McMakin, H. D. Collins, T. E. Hall, and R. H. Severtsen, "Concealed explosive detection on personnel using a wideband holographic millimeter-wave imaging system," *Proceedings of SPIE*, Vol. 2755, 503–513, 1996.
16. Sheen, D., D. McMakin, and T. Hall, "Near-field three-dimensional radar imaging techniques and applications," *Applied Optics*, Vol. 49, E83–E93, Jun. 2010.
17. Tan, W., W. Hong, Y. Wang, and Y. Wu, "A novel spherical-wave three-dimensional imaging algorithm for microwave cylindrical scanning geometries," *Progress In Electromagnetics Research*, Vol. 111, 43–70, 2011.
18. Soumekh, M., "Reconnaissance with slant plane circular SAR imaging," *IEEE Trans. on Image Process*, Vol. 5, 1252–1265, 1996
19. Soumekh, M., *Synthetic Aperture Radar Signal Processing with MATLAB Algorithm*, John Wiley & Sons, New York, 1999
20. Guo, D., H. Xu, and J. Li, "Extended wavenumber domain algorithm for highly squinted sliding spotlight SAR data processing," *Progress In Electromagnetics Research*, Vol. 114, 17–32, 2011.
21. Fortuny, J. and J. M. L'opez-S'anchez, "Extension of the 3-D range migration algorithm to cylindrical and spherical scanning geometries," *IEEE Trans. on Antennas and Propagation*, Vol. 49, 1434–1444, 2001.
22. Carrara, W. G., R. S. Goodman, and R. M. Majewski, *Spotlight Synthetic Aperture Radar Signal Processing Algorithms*, Artech House, Boston, MA, 1995.
23. Franceschetti, G. and R. Lanari, *Synthetic Aperture Radar Processing*, CRC Press, Boca Raton, FL, 1999.
24. Cumming, I. G. and F. H. Wong, *Digital Processing of Synthetic Aperture Radar Data Algorithms and Implementation*, Artech House, Norwood, MA, 2005.
25. Li, S., B. Ren, H.-J. Sun, W. D. Hu, and X. Lv, "Modified wavenumber domain algorithm for three-dimensional millimeter-wave imaging," *Progress In Electromagnetics Research*, Vol. 124, 35–53, 2012.